ELSEVIER

J. Non-Newtonian Fluid Mech. 152 (2008) 86–100

Journal of Non-Newtonian Fluid Mechanics

www.elsevier.com/locate/jnnfm

An examination of droplet deformation and break-up between concentrically rotating cylinders

Marco Dressler [a,*], Brian J. Edwards [b], Erich J. Windhab [a]

[a] *Institute of Food Science and Nutrition, Laboratory of Food Process Engineering, ETH-Zürich, CH-8092 Zürich, Switzerland*
[b] *Department of Chemical and Biomolecular Engineering, University of Tennessee, Knoxville, TN 37996, United States*

Received 30 November 2006; received in revised form 3 October 2007; accepted 29 October 2007

Abstract

A thermodynamically consistent polymer blend model was solved numerically to understand the isothermal flow of these complex fluids in the annular gap between rotating concentric cylinders. Calculations were performed at various gap widths and differing speeds when the cylinders were rotating in the same and opposite directions. The aim of this exercise was to determine the optimal operating conditions under which droplet break-up would dominate over coalescence during the flow process, thus producing a nearly homogeneous distribution of very small droplets.

Keywords: Immiscible polymer blends; Rotating cylinders; Droplet break-up and coalescence

1. Introduction

The development of novel polymers with superior material properties has always been an expensive and time-consuming process. Over the previous two decades, it has become standard practice to avoid this issue by blending two or more standard industrial polymers together to form an immiscible mixture to produce new and improved products with tailored rheological and morphological properties. This too, however, is an expensive and time-consuming process of trial and error. The primary reason for the expense and time consumption is that there currently exists no industry-standard, working model of immiscible polymer blends, which would allow intelligent, design-oriented simulations of polymer blend properties and morphological characteristics. Such simulations would dramatically reduce the cost and inefficiency of polymer blend tailoring, and thus significantly improve the capability of industrial engineers to design novel polymer blends with suitable properties necessary for a particular application.

Over the past decade, theoreticians began to develop simple models for the dynamical properties of fluids composed of immiscible blends. The first model to describe some of the basic properties of blends was introduced by Doi and Ohta in 1991 [1]. Since then, several additional models have been developed, each with an increasing degree of sophistication [2–7]. For instance, Wagner et al. [2] produced the first thermodynamically consistent model of blends. Maffettone and Minale [3] developed the first blend model that conserved droplet volume. Dressler and Edwards derived a model with a viscoelastic matrix phase [5], and accounted for the coalescence and break-up of droplets under flow [6]. These and other models have laid the foundation for future advances in the study of flows of immiscible blends, but still, not much effort has been expended to examine the predictions of these models under industrially relevant flow conditions. Basic calculations with these models are usually performed under idealistic flow conditions, such as homogeneous shear or uniaxial extensional flow. However, recent advances in numerical methodology [8,9] have made possible calculations with these sophisticated models under inhomogeneous flow fields that are relevant to the polymer processing industry [10].

Now that real processing geometries can be simulated with these models, it is time to test their predictive power by performing flow calculations in specific flow geometries of industrial concern, especially those which are easily reproduced in a laboratory or process setting. In this article, we begin this process by examining flow of a generic blend between concentric cylinders, rotating in the same or opposite directions. Specifically,

* Corresponding author.
E-mail address: marco.dressler@ilw.agrl.ethz.ch (M. Dressler).

0377-0257/$ – see front matter © 2007 Elsevier B.V. All rights reserved.
doi:10.1016/j.jnnfm.2007.10.022

we want to answer the following question, which is particularly relevant to industrial processes. How can the microstructure of immiscible viscoelastic fluids be tailored to produce blends with many very small, deformed, and uniformly oriented droplets using concentric cylinder devices? This is particularly relevant since most industrial engineers would like to produce blends for processing which have the maximum number of droplets, with specific orientations, in order to obtain the optimal material properties from the blended polymers.

Studies on deformation and break-up of isolated Newtonian droplets in a Newtonian matrix have a long tradition, beginning with theoretical and experimental work for steady [11] and transient homogeneous flows [12]. Later, droplet interactions in blends of Newtonian liquids were taken into account explicitly to model non-dilute systems [13]. Furthermore, early studies [14] on capillary instabilities of fluid threads under idealized conditions were developed [15] to take into account Newtonian flow behavior of the phases, as well as a constant extension rate of the surrounding fluid. Theories of droplet deformation and capillary jet break-up have been reconsidered and compared with experimental data over extended regimes of blend parameters (viscosity ratio, interfacial tension) and for creeping flow conditions in Ref. [16] to predict dispersion performance of static mixers. Blends of non-Newtonian fluids were studied in Ref. [17].

In the following section, we will introduce the thermodynamically consistent blend model to be used in this examination. Afterward, we will discuss the numerical methodology that is used to solve the model equations in the concentric cylinder geometry. Sample results are presented in the following section, with the aim of determining the optimal conditions for producing the greatest number of deformed and oriented droplets in this geometry. Conclusions are presented in the final section.

2. The thermodynamically consistent blend model

We assume that the rheology and microstructure of the blend is described appropriately in terms of the mass density, $\rho(\mathbf{r}, t)$, the momentum density, $\mathbf{M}(\mathbf{r}, t)$, the contravariant second-rank conformation tensor, $\mathbf{C}(\mathbf{r}, t)$, the contravariant second-rank droplet shape tensor, $\mathbf{S}(\mathbf{r}, t)$ (with $\det \mathbf{S} = 1$), and the number density of micro-droplets, $n(\mathbf{r}, t)$. Mass density and momentum density are macroscopic variables describing the effective density and momentum of the blend, viewed as a macroscopic thermodynamic system. The conformation tensor, droplet shape tensor, and number density are internal variables describing the blend microstructure. A set of dynamic equations for the five fields can then be derived from non-equilibrium thermodynamics according to the master equation [18–21]

$$\frac{\mathrm{d}F}{\mathrm{d}t} = \{F, H\} + [F, H]. \tag{1}$$

In this equation, F is an arbitrary functional of the five fields introduced above, $\mathrm{d}\cdot/\mathrm{d}t$ is the derivative of a functional with respect to time, and H is the Hamiltonian. The French and square brackets denote the Poisson and dissipation brackets, respectively. They quantify the reversible and irreversible dynamics of the functional F. In Ref. [6], we used Eq. (1) to derive a set of flow equations for the dynamic variables mentioned above. The scope of this article is to solve these flow equations for steady flows in the annular gap between concentrically rotating cylinders.

For the Hamiltonian of the polymer blend, we make the following constitutive assumption [6]

$$\begin{aligned} H_{\mathrm{m}}[\mathbf{M}, \mathbf{C}, \mathbf{S}, n] &= K[\mathbf{M}] + A[\mathbf{C}, \mathbf{S}, n] \\ &= \int \left[\frac{M_\alpha M_\alpha}{2\rho} + \frac{1}{2}(1-\phi) G \frac{K}{k_{\mathrm{B}}T} I_1^{\mathrm{C}} \right. \\ &\quad - \frac{1}{2}(1-\phi) G \ln\left(\det \frac{K\mathbf{C}}{k_{\mathrm{B}}T}\right) + \frac{1}{2}\phi\Gamma\frac{n}{n_0} I_2^{\mathrm{S}} \\ &\quad \left. - \frac{1}{6}\phi\Gamma\frac{K}{k_{\mathrm{B}}T} \ln\left(\frac{n}{n_0}\right) I_1^{\mathrm{C}} \epsilon(I_1^{\mathrm{S}}, I_2^{\mathrm{S}}) \right] \mathrm{d}^3x, \end{aligned} \tag{2}$$

where the integration is performed over the constant total system volume. In this equation, ϕ is the volume fraction of the dispersed phase, G is the elastic modulus of the matrix phase, K is the characteristic elastic constant of matrix molecules, Γ is the elastic modulus of the droplet interface, n_0 is the number density of micro-droplets in the quiescent state, and I_i^{X} ($\mathbf{X}$ is either $\mathbf{C}$ or $\mathbf{S}$) is the ith scalar invariant of the conformation tensor or the droplet shape tensor. The first term in the integral is the kinetic energy of the blend, the second and third terms account for the elastic energy of the matrix phase, the fourth term represents the elastic energy of the interface, and the last term is a mixing term to model elastic droplet/matrix interactions. The Hamiltonian of Eq. (2) does not take into account droplet–droplet interactions that depend on average separation.

As in the Doi–Ohta Model [1], we use a tensorial and a scalar variable to describe the dispersed phase microstructure. The Doi–Ohta Model was formulated in terms of a covariant second-rank tensor and a scalar variable. They quantify the orientation/deformation of the interface and the amount of interfacial area in a co-continuous system [1] or in a system with droplet morphology [7]. Thus, the Doi–Ohta variables describe phase inversion if this process passes through a co-continuous state, although the description of droplet shapes in terms of the Doi–Ohta variables is awkward [7]. The Hamiltonian (2) is written in terms of a contravariant second-rank tensor to describe deformation and orientation of droplets, and a scalar variable for the number density of droplets. With this interpretation of the variables, it is not possible to describe phase inversion or co-continuous systems. It is not clear whether a different interpretation of the contravariant, second-rank tensor $\mathbf{S}$ and the scalar variable n would allow description of the co-continuous and dispersed phase systems.

For steady, fully developed, and incompressible flow, the set of time evolution equations derived in Ref. [6] is

$$\operatorname{tr}\mathbf{L} = 0, \tag{3a}$$

$$-\rho\mathbf{v}\cdot\nabla\mathbf{v} - \nabla p + \nabla\cdot\boldsymbol{\sigma} = 0, \tag{3b}$$

$$-\mathbf{v}\cdot\nabla\mathbf{C}+\mathbf{C}\cdot\mathbf{L}^{\mathrm{T}}+\mathbf{L}\cdot\mathbf{C}-(1-\phi)\frac{1}{\lambda_{\mathrm{C}}}\left(\frac{I_1^{\mathrm{C}}}{3}\right)^{-k}\left(\mathbf{C}-\frac{k_{\mathrm{B}}T}{K}\mathbf{1}\right)$$
$$+\frac{1}{3}\phi\frac{\Gamma}{G}\frac{1}{\lambda_{\mathrm{C}}}\left(\frac{I_1^{\mathrm{C}}}{3}\right)^{-k}\ln\left(\frac{n}{n_0}\right)I_1^{\mathrm{S}}\mathbf{C}$$
$$-\frac{1}{2}\sqrt{\frac{\Gamma}{G}}(1+p^{\star})^2\phi\theta\frac{1}{\sqrt{\lambda_{\mathrm{C}}\lambda_{\mathrm{S}}}}\left(\frac{I_1^{\mathrm{C}}}{3}\right)^{-k/2}$$
$$\times\left\{\frac{n}{n_0}\left[I_1^{\mathrm{S}}(\mathbf{C}\cdot\mathbf{S}+\mathbf{S}\cdot\mathbf{C})-(\mathbf{C}\cdot\mathbf{S}\cdot\mathbf{S}+\mathbf{S}\cdot\mathbf{S}\cdot\mathbf{C})-\frac{4}{3}I_2^{\mathrm{S}}\mathbf{C}\right]\right.$$
$$\left.-\frac{1}{3}\frac{K}{k_{\mathrm{B}}T}\ln\left(\frac{n}{n_0}\right)I_1^{\mathrm{C}}\left(\mathbf{C}\cdot\mathbf{S}+\mathbf{S}\cdot\mathbf{C}-\frac{2}{3}I_1^{\mathrm{S}}\mathbf{C}\right)\right\}=0, \tag{3c}$$

$$-\mathbf{v}\cdot\nabla\mathbf{S}-\frac{2}{3}\mathrm{tr}\,\mathbf{L}\,\mathbf{S}+\mathbf{S}\cdot\mathbf{L}^{\mathrm{T}}+\mathbf{L}\cdot\mathbf{S}$$
$$-(1+p^{\star})^2p^{\star}\phi\frac{1}{\lambda_{\mathrm{S}}}\frac{n}{n_0}\left(\frac{1}{3}I_1^{\mathrm{S}}\mathbf{S}-\mathbf{S}\cdot\mathbf{S}\right)$$
$$+p^{\star}\phi\frac{1}{\lambda_{\mathrm{S}}}\left[\frac{n}{n_0}-\frac{1}{3}\frac{K}{k_{\mathrm{B}}T}\ln\left(\frac{n}{n_0}\right)\frac{I_1^{\mathrm{C}}}{I_1^{\mathrm{S}}}\right]\left(\mathbf{S}-\frac{3}{I_2^{\mathrm{S}}}\mathbf{1}\right)$$
$$-\frac{1}{2}(1+p^{\star})^2\theta\frac{1}{\sqrt{\lambda_{\mathrm{C}}\lambda_{\mathrm{S}}}}\frac{K}{k_{\mathrm{B}}T}\left(\frac{I_1^{\mathrm{C}}}{3}\right)^{-k/2}$$
$$\times\left[(1-\phi)\sqrt{\frac{G}{\Gamma}}-\frac{\phi}{3}\sqrt{\frac{\Gamma}{G}}\ln\left(\frac{n}{n_0}\right)I_1^{\mathrm{S}}\right]$$
$$\times\left(\mathbf{C}\cdot\mathbf{S}+\mathbf{S}\cdot\mathbf{C}-\frac{2}{3}I_1^{\mathrm{C}}\mathbf{S}\right)=0, \tag{3d}$$

$$-\mathbf{v}\cdot\nabla n-\phi f_{\mathrm{c}}I_2^{\mathrm{S}}\frac{1}{\lambda_{\mathrm{n}}}\frac{n}{n_0}+\frac{\phi f_{\mathrm{c}}I_1^{\mathrm{C}}I_1^{\mathrm{S}}}{3}\frac{K}{k_{\mathrm{B}}T}\frac{1}{\lambda_{\mathrm{n}}}=0, \tag{3e}$$

where $\mathbf{v}=\mathbf{M}/\rho$ is the velocity field and $\mathbf{L}=(\nabla\mathbf{v})^{\mathrm{T}}$ is the transpose of the velocity gradient tensor. As already mentioned, Eq. (3) is field equation for steady flow. To obtain the full set of dynamic equations [6], Eq. (3a), should be replaced with the continuity equation for ρ and the right side of Eqs. (3b)–(3e) should be replaced with the local derivatives of the variables $\mathbf{v}$, $\mathbf{C}$, $\mathbf{S}$, and n, respectively. These equations are examined in Section 4 under an imposed inhomogeneous shear flow between concentrically rotating cylinders.

Eq. (3a) is the continuity equation for an incompressible medium. Eq. (3b) is the Cauchy momentum balance for steady, fully developed flow, where $\mathbf{v}\cdot\nabla\mathbf{v}$ is the non-vanishing contribution to the material derivative, ∇p is the pressure gradient, and $\nabla\cdot\boldsymbol{\sigma}$ is the divergence of the extra stress tensor. The velocity field has dimensions of (length/time), the pressure and extra stress tensor fields of (energy/length^3), and the density of (mass/length^3). The constitutive equation for the extra stress tensor that renders the microstructural Eqs. (3c)–(3e) thermodynamically consistent with the Cauchy momentum balance is [6]

$$\boldsymbol{\sigma}=(1-\phi)G\left(\frac{K}{k_{\mathrm{B}}T}\mathbf{C}-\mathbf{1}\right)+\phi\Gamma\frac{n}{n_0}\left(I_1^{\mathrm{S}}\mathbf{S}-\mathbf{S}\cdot\mathbf{S}-\frac{2}{3}I_2^{\mathrm{S}}\mathbf{1}\right)$$
$$-\frac{\phi}{3}\Gamma\frac{K}{k_{\mathrm{B}}T}\ln\left(\frac{n}{n_0}\right)\left(I_1^{\mathrm{C}}\mathbf{S}+I_1^{\mathrm{S}}\mathbf{C}-\frac{1}{3}I_1^{\mathrm{C}}I_1^{\mathrm{S}}\mathbf{1}\right). \tag{3f}$$

The first two terms represent contributions from matrix viscoelasticity and droplet deformation, respectively. The third term is a contribution from droplet break-up/coalescence. Note that Eq. (3f) implies that $\boldsymbol{\sigma}=\boldsymbol{\sigma}^{\mathrm{T}}$ is a symmetric, second-rank tensor. Eq. (3f) holds for both steady and transient flows.

Eq. (3c) is the conformation tensor equation describing steady flow of the matrix phase microstructure. The conformation tensor, $\mathbf{C}$, has units of (length)^2 and it is rendered dimensionless with $K/k_{\mathrm{B}}T$, where K is the characteristic elastic constant and $k_{\mathrm{B}}T$ is the thermal energy. Since K is related to the second moment of the end-to-end vector averaged over all configurations, there is a direct microstructural interpretation of $\mathbf{C}$ based on the principles of statistical mechanics. In Eq. (3c), we have introduced λ_{C} as the relaxation time related to the long end of the spectrum of the viscoelastic matrix fluid, k as a power law index according to the Extended White Metzner Model [22], $p^{\star}=-\eta_{\mathrm{d}}/\eta_{\mathrm{c}}$ as the negative viscosity ratio of the phases [5], and θ as a phenomenological coupling parameter which accounts for the influence of droplet deformation on matrix microstructure. The first three terms originate from the Poisson bracket in Eq. (1), and represent Oldroyd's contravariant deformational derivative of the conformation tensor, $\mathbf{C}$. The last three terms are irreversible contributions derived from the dissipation bracket in Eq. (1). The fourth term describes relaxation of the matrix molecules, and the last two terms account for the influence of break-up/coalescence events and droplet deformation on the matrix fluid conformation.

Eq. (3d) is the droplet shape tensor evolution equation. The droplet shape tensor, $\mathbf{S}$, appearing in Eq. (3d), is a dimensionless second-rank tensor. The reason is that Eq. (3d) is constructed with the mapping $\mathbf{B}\rightarrow\mathbf{B}/(\det\mathbf{B})^{1/3}\equiv\mathbf{S}$ from the Poisson and dissipation brackets for an unconstrained droplet shape tensor ($\mathbf{B}$), with dimension (length)^2. The length scale related to the droplet shape tensor, $\mathbf{B}$, is independent of the length scale of the conformation tensor, $\mathbf{C}$. In Eq. (3d), λ_{S} is a relaxation time related to the elastic interface and θ accounts for the effect of matrix phase deformation on droplet shape. Again, the first four terms originate from the Poisson bracket and are related to Oldroyd's contravariant derivative of the second-rank tensor $\mathbf{S}$, under the constant volume constraint, $\det\mathbf{S}=1$ [23]. The last three terms are irreversible contributions, which quantify the effect of flow, droplet break-up/coalescence, and matrix microstructural dynamics on drop shape.

Eq. (3e) is the droplet number density evolution equation for the droplet number density with dimension (length)$^{-3}$, where f_{c} is a phenomenological parameter which accounts for the probability of a coalescence process and λ_{n} is a characteristic time scale that is related to the break-up/coalescence events. The first term in Eq. (3e) is the material derivative derived from the Poisson bracket, and the remaining two terms are irreversible

contributions stemming from the dissipation bracket. The second term accounts for a decrease (coalescence) and the third term accounts for an increase of the number density of droplets (break-up).

Eq. (3) represent a set of coupled, non-linear partial differential equations. Therefore, numerical techniques are required to obtain physically meaningful solutions of these equations. A simple analytical solution of the model equations may be obtained for the quiescent polymer blend, $\boldsymbol{\sigma} = \mathbf{0}$. In this case, $\mathbf{L} = \mathbf{0}$, which implies $\mathbf{C} = (k_B T/K)\mathbf{1}$, $\mathbf{S} = \mathbf{1}$, and $n = n_0$; i.e., the polymer blend is in the undeformed state.

3. Numerical methodology

The blend model of Eq. (3) was solved in the annular gap between two concentric cylinders with inner radius, R_i, and outer radius, R_o. The ratio of cylinder radii is $\kappa = R_i/R_o$, and the annular gap is $\delta = R_o - R_i$. The relative distance from the inner cylinder is $\bar{r} = (r - R_i)/(R_o - R_i)$. To solve the polymer blend model for this flow geometry, we adopt cylindrical coordinates (r, φ, z), where r is the radial distance from the common cylinder axis, φ is the angular coordinate, and z is the coordinate along the cylinder axis.

We assume that there is no motion of the blend in the radial direction and that flow is laminar. Then the velocity field is of the form

$$\mathbf{v} = (0, v_\varphi(r), 0)^T, \tag{4}$$

which satisfies the no-penetration conditions imposed by the confining cylinders. Furthermore, we assume that the properties of the cylinders are such that slip does not occur. This implies that the velocity field (4) satisfies the no-slip boundary conditions

$$v_\varphi(r = R_i) = U_i, \tag{5a}$$

$$v_\varphi(r = R_o) = U_o, \tag{5b}$$

where U_i and U_o are the inner and outer cylinder velocities, respectively. If one of the cylinders is stationary, the right side of the respective contribution to Eq. (5) vanishes.

The set of partial differential equations (3) is written in terms of dimensional quantities. To obtain dimensionless quantities, we use the definitions $\mathbf{C} = k_B T\tilde{\mathbf{C}}/K$, $n = n_0\tilde{n}$, $\boldsymbol{\sigma} = \sqrt{G\Gamma}\ \tilde{\boldsymbol{\sigma}}$, $p = \sqrt{G\Gamma}\ \tilde{p}$, and $\mathbf{L} = \tilde{\mathbf{L}}/\sqrt[3]{\lambda_C\lambda_S\lambda_n}$. The spatial coordinate, $\mathbf{r}$, is rendered dimensionless according to $\mathbf{r} = \delta\tilde{\mathbf{r}}$, where δ is the characteristic length scale of the flow, which is the gap width of the annulus. Note that the droplet shape tensor, as introduced with the set of thermodynamic variables, is a dimensionless quantity; i.e., $\mathbf{S} = \tilde{\mathbf{S}}$. To obtain a droplet dimension from $\mathbf{S}$ one can use the mass conservation and incompressibility of the dispersed phase to calculate an average droplet radius for the deforming polymer blend, i.e., $R_n = (n_0/n)^{1/3}R_0$, where R_0 is the average droplet radius in the undeformed state and R_n is the average droplet size for a blend with n droplets per unit volume. With this definition, the length scale associated with $\mathbf{S}$ is not constant, but it increases or decreases in conjunction with the coalescence or break-up processes. The three length scales are made dimensionless with the three independent quantities δ, $(K/k_B T)^{1/2}$, and $R_n \equiv (\det \mathbf{B})^{1/6}$, and the velocity gradient is made dimensionless with the geometric mean value of the three relaxation times, λ_C and λ_S, λ_n. Alternatively, one can use the geometric mean length scale $(\delta^2 K/k_B T\ R_n^2)^{1/6}$ to associate this single length scale to the gap width and to the microstructural variables $\mathbf{C}$, $\mathbf{S}$. Using the geometric mean value of the relaxation times to render dimensionless velocity gradient, and distinct length scales to render dimensionless the microstructural variables, is qualitatively the same procedure as described in Ref. [18]. Indeed, in Ref. [18], the relevant length scale for each microstructural variable is used to render dimensionless conformation tensors in multi-mode viscoelastic fluid models. In all that follows, we use these dimensionless quantities and drop the tilde which denotes them.

Having introduced dimensionless quantities and assumed laminar flow, we express the flow equations, (3), in cylindrical coordinates. It is apparent that Eq. (4) satisfies the divergence-free condition, (3a), in cylindrical coordinates, $\mathrm{tr}\,\mathbf{L} = 0$. The radial, angular, and axial components of Cauchy's momentum balance, (3b), in cylindrical coordinates, are

$$-Ta\frac{v_\varphi^2}{r} = \frac{1}{r}\frac{\partial}{\partial r}(r\sigma_{rr}) - \frac{\sigma_{\varphi\varphi}}{r} - \frac{\partial p}{\partial r}, \tag{6a}$$

$$0 = \frac{1}{r^2}\frac{\partial}{\partial r}(r^2\sigma_{r\varphi}), \tag{6b}$$

$$0 = \frac{1}{r}\frac{\partial}{\partial r}(r\sigma_{rz}), \tag{6c}$$

since the extra stress tensor is symmetric and it is a function of the radial coordinate only. In Eq. (6a), the Taylor number, $Ta = \rho^2(U_i - U_o)^2\delta^3/(R_i G\lambda_C\Gamma\,\lambda_S)$, is obtained by rendering dimensionless momentum balance (3b). The term v_φ^2/r is a non-trivial contribution from the convective derivative $\mathbf{v}\cdot\nabla\mathbf{v}$ in cylindrical coordinates, with $\mathbf{v}$ given by Eq. (4). Eq. (6a) expresses the balance of centrifugal forces proportional to v_φ^2 with the variation of radial normal stresses, the first normal stress difference, and the radial pressure distribution. From Eqs. (6b) and (6c), we see immediately that the radial angular shear stress and the radial axial shear stress are proportional to r^{-1} and r^{-2}, respectively.

Next we consider the reversible contributions to the conformation tensor equation, (3c), and the droplet shape tensor equation, (3d). Note that the form of the irreversible contributions is independent of the coordinate system, since these terms do not contain spatial derivatives. Therefore, it suffices to inspect the reversible contributions of these equations. The reversible terms in the $\mathbf{C}$ and $\mathbf{S}$ equations are of the same form, since the flow is incompressible. In cylindrical coordinates [24],

$$\mathbf{v}\cdot\nabla\mathbf{X} - \mathbf{X}\cdot\mathbf{L}^T - \mathbf{L}\cdot\mathbf{X} = \hat{Q}\,\mathbf{X} + \frac{v_\varphi}{r}\mathbf{M} - \mathbf{X}\cdot\mathbf{L}^T - \mathbf{L}\cdot\mathbf{X}, \tag{7}$$

where $\mathbf{X}$ is either $\mathbf{C}$ or $\mathbf{S}$. In this expression, $\hat{Q} = v_r\partial_r + v_\varphi/r\partial_\varphi + v_z\partial_z$ is a differential operator,

$$\mathbf{M} = \begin{pmatrix} -2X_{r\varphi} & X_{rr} - X_{\varphi\varphi} & 0 \\ * & 2X_{r\varphi} & X_{rz} \\ * & * & 0 \end{pmatrix}, \tag{8}$$

is a matrix with $*$ denoting a symmetric entry, and $\mathbf{L}$ is the velocity gradient tensor in cylindrical coordinates. For rotating flow, the vanishing radial fluid motion implies $\hat{Q} = 0$, and the velocity gradient has only two non-trivial entries:

$$\mathbf{L} = \begin{pmatrix} 0 & -\dfrac{v_\varphi}{r} & 0 \\ \dfrac{\partial v_\varphi}{\partial r} & 0 & 0 \\ 0 & 0 & 0 \end{pmatrix}. \tag{9}$$

The magnitude of the velocity gradient $\dot{\gamma} = 2\sqrt{-II_{\mathbf{D}}}$, $II_{\mathbf{D}}$ being the second invariant of the rate-of-deformation tensor $\mathbf{D} = 1/2(\mathbf{L} + \mathbf{L}^{\mathrm{T}})$, is a measure of the shear rate [25]. For the velocity gradient of Eq. (9), we have thus

$$\dot{\gamma} = \frac{\partial v_\varphi}{\partial r} - \frac{v_\varphi}{r} \tag{10}$$

for the shear rate of circular Couette flow.

Eq. (4) implies that the conformation tensor, droplet shape tensor, droplet number density, and the extra stress tensor are functions of the radial coordinate, r. Since all variables depend on one spatial coordinate only, and the flow is stationary, the set of partial differential equations (3a–3f) reduces to a set of ordinary differential equations (ODEs),

$$\mathcal{A} \cdot \boldsymbol{\xi}' = \mathbf{b}, \tag{11}$$

which was solved for the boundary conditions (5). In the above linear equation, $\boldsymbol{\xi}$ is a 12-tuple of the non-trivial physical fields, $\mathcal{A}$ is a 12×12 coefficient matrix, $\mathbf{b}$ is a 12-tuple called the "inhomogeneity," and "$'$" denotes differentiation with respect to the radial coordinate, r. The coefficient matrix, $\mathcal{A}$, and the inhomogeneity, $\mathbf{b}$, are obtained from the continuum equations (3). For laminar flow,

$$\boldsymbol{\xi} = (p, v_\varphi, v'_\varphi, \mathrm{vec}(\mathbf{C}), \mathrm{vec}(\mathbf{S}), n)^{\mathrm{T}}, \tag{12}$$

where $v'_\varphi = \partial v_\varphi/\partial r$, is the derivative of the velocity field, and $\mathrm{vec}(\mathbf{X}) = (X_{rr}, X_{r\varphi}, X_{\varphi\varphi}, X_{zz})$ with $\mathbf{X}$ being either $\mathbf{C}$ or $\mathbf{S}$. To obtain the solutions to these equations, $\boldsymbol{\xi}$, the set of ODE's (11) is solved between the inner and outer cylinders.

The coefficient matrix, $\mathcal{A}$, and the inhomogeneity, $\mathbf{b}$, in Eq. (11) were obtained in the following manner. The first row of $(\mathcal{A}, \mathbf{b})$ corresponding to p is the r-component of Cauchy's momentum balance in cylindrical coordinates (6a). The second and third rows of $(\mathcal{A}, \mathbf{b})$ corresponding to v_φ and v'_φ are the φ-component of the momentum balance equation, (6b), and the $r\varphi$-component of the conformation tensor equation, respectively. The remaining nine rows of $(\mathcal{A}, \mathbf{b})$, corresponding to the non-trivial components of the microstructural variables and to the number density of the droplets, are identified by taking the derivative of the microstructural variable in Eqs. (3c) and (3d), and of the number density Eq. (3e), with respect to r.

The two-point boundary value (TPBV) problem for the annular gap, i.e., the set of ODEs (11) together with the boundary conditions (5), was solved computationally using a shooting algorithm. The shooting algorithm uses a fourth-order Runge–Kutta scheme with adaptive step size to integrate the set of ODEs between the inner and outer cylinders, and a globally convergent Newton algorithm to match the no-slip conditions (5) on the outer cylinder. The shooting algorithm and the other numerical routines used in this study were taken from Ref. [26].

The TPBV problem was solved for given cylinder velocities U_{i} and U_{o}. The linear system (11) was solved using an LU decomposition of the coefficient matrix, $\mathcal{A}$. Then the set of ODEs $\boldsymbol{\xi}' = \mathcal{A}^{-1} \cdot \mathbf{b}$ was integrated using the Runge–Kutta algorithm shooting from the inner cylinder, $r = R_{\mathrm{i}}$, to the outer one, $r = R_{\mathrm{o}}$. Each Runge–Kutta integration began with the same initial condition (5a) on the velocity flow field, and with different values of the derivative $v'_\varphi(r)$ on the inner cylinder acting as the independent variables of the Newton subroutine in the shooting algorithm. The Runge–Kutta integrations were repeated until the Newton algorithm converged; i.e., until the boundary condition (5b) on the outer cylinder was satisfied. Prior to each Runge–Kutta application, the homogeneous shear flow problem related to Eq. (3) was solved for the velocity gradient tensor (9), because the microstructural characteristics at the inner cylinder were non-trivial functions of $\mathbf{L}$. This was necessary because the flow problem possessed no symmetry. To solve the steady shear flow problem at the inner cylinder, we used a 12-dimensional Newton–Raphson algorithm to obtain the microstructural characteristics. This generalized the steady shear flow solution technique of Ref. [8] to cylindrical coordinates. The consistency of the new algorithm with the algorithms in Ref. [8,9] was checked carefully.

4. Sample results

In the model Eq. (3), we assumed the value $\phi = 0.1$ for the dispersed phase volume fraction, since we expect that the results of this study will be more or less qualitatively equivalent for the small range of ϕ values for which these equations are applicable. The probability f_{c} was assigned the value of unity, since we are more interested in the variations of the other system variables in this particular case. The elastic moduli ratio of $G/\Gamma = 4$ was examined as one key parameter to determine the relative energies of the polymer blend components. This parameter can allow a rational choice to be made for the best components to produce the final desired microstructure. The relaxation times studied were $\lambda_{\mathrm{C}} = \lambda_{\mathrm{S}} = \lambda_{\mathrm{n}} = 1$. Obviously, these parameter values can affect the model results, however, we concentrated on variations of other interesting quantities in this article due to restrictions on length. The coupling coefficient was taken as $\theta = 0.1$, and the power-law index was assumed to be $k = -2$, since neither of these parameters should affect the qualitative features of the results. We performed sample calculations for two polymer blends with different viscosity ratios, $p^\star = -1.25$ and -0.25, again, so that the choice of the blend

components can be made rationally. For the size of the annulus, we set $R_i = 0.3$, 0.5, and 0.7, and $R_o = 1$ for the inner and outer cylinders, respectively. This assigns the values of κ to be 0.3, 0.5, and 0.7. Note that $\kappa = 0.3$ is the widest gap, and that $\kappa = 0.7$ is the most narrow. We considered three rotation cases for the cylinders: inner cylinder rotation, co-rotating cylinders, and counter-rotating cylinders. We determined the velocity field, microstructure, and stress profiles for the material and geometry parameters specified above.

To recover physical blend properties from the calculations, one has to define three time scales and three length scales for the fluid, i.e., λ_C, λ_S, λ_n and δ, $(K/k_BT)^{1/2}$, and R_0. These time and length scales are all independent of each other. If one wants to assume a quasi-equilibrium approximation, then in particular $\delta \ll R_0$, i.e., drops are orders of magnitude smaller than the gap width.

4.1. Inner cylinder rotation

4.1.1. Small viscosity ratio blends

Fig. 1a presents the circular velocity field for the small viscosity ratio blend, $p^\star = -0.25$, for the cylinder gap $\kappa = 0.3$. The circular velocity is a decreasing function of the radial coordinate, as expected. The velocity near the rotating inner cylinder possesses a higher value than near the stationary outer cylinder due to the no-slip boundary condition. The four rotational speeds of the inner cylinder that were examined can be identified from the ordinate in Fig. 1a. The derivative of the velocity field, $v'_\varphi = \partial v_\varphi/\partial r$, displayed in Fig. 1b, is a monotonically decreasing function of radial position, again as expected from the no-slip boundary condition. Also, the strong variation of this derivative near the inner cylinder and slow decrease near the outer cylinder is as expected. The shear rate profile is easily calculated from the profiles of v_φ and v'_φ, which are obtained from the shooting algorithm. Fig. 1c shows the shear rate, Eq. (10), which, for this type of flow and model parameters, is of the same order of magnitude and shows the same qualitative behavior as the derivative of the velocity field. We remark that the shear rates in the gap vary over a range of approximately two orders of magnitude. Note that the derivative of the velocity field and the shear rate do not vanish on the outer cylinder. This leads to a non-trivial droplet configuration, as shown in Fig. 2.

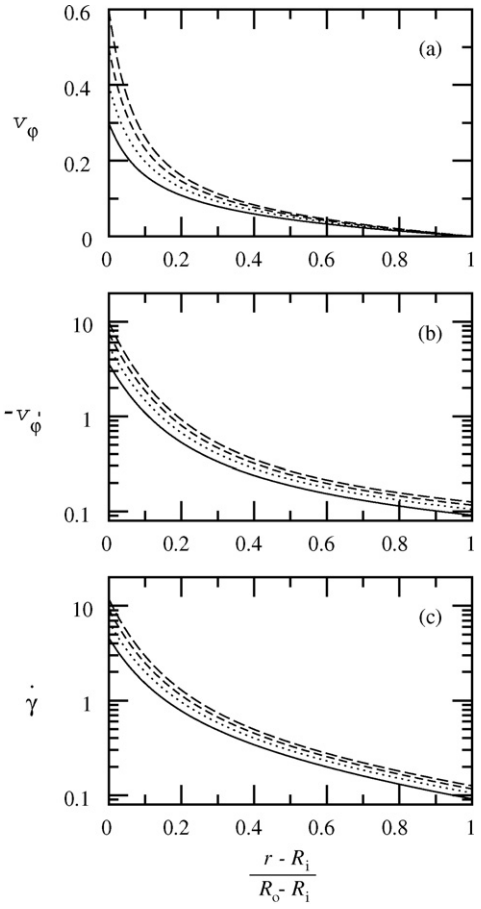

Fig. 1. Couette flow profiles for the $p^* = -0.25$ polymer blend in the annular gap $\kappa = 0.3$ for four inner cylinder velocities: $U_i = 0.3$ (solid lines), 0.4 (dotted lines), 0.5 (dashed lines), and 0.6 (long-dashed lines). Other model parameters are $\phi = 0.1$, $G/\Gamma = 4$, $\lambda_C\lambda_S/\lambda_n^2 = 1$, $\theta = 0.1$, and $k = -2$. (a) Circular velocity, (b) derivative of the circular velocity, and (c) corresponding shear rate.

The Reynolds number of the flow problem can be defined in analogy to the Taylor number, Eq. (6a), as $Re = (U_i - U_o)\delta\rho/\sqrt{G\lambda_C\Gamma\lambda_S}$. However, since we have not specified physical data for the polymer blends, we cannot determine the Reynolds and Taylor numbers. Evaluating the Reynolds number for dimensionless values, together with $\rho = 1$, $G = 4$, yields a value smaller than unity, as expected for highly viscous polymer blends.

Concentric cylinder flow of elastic fluids becomes unstable if the Deborah number, $De = (U_i - R_iU_o/R_o)\sqrt[3]{\lambda_C\lambda_S\lambda_n}/\delta$, exceeds a critical value, cf. e.g., Ref. [27]. The onset of elastic instabilities depends on the viscometric material properties and their dependence on the rate of deformation; i.e., the power-law behavior of the zero shear viscosity, the normal stress coefficients, and their ratio. Evaluation of the Deborah number for the flows of Fig. 1 gives values on the order of unity. However, as seen from Fig. 1c, the shear rates on the inner cylinder are large compared to the ratio U_i/δ. Therefore, we believe that for the model studied herein, evaluation of the Deborah number does not admit conclusions on the stability of the calculated flow fields. This is corroborated also by the fact that the microstructural Eqs. (3c)–(3e) and the constitutive equation for the elastic stresses (3f) are highly non-linear. In the following, we assume explicitly stability of the flow; i.e., small perturbations of the velocity field and of the microstructural characteristics decay exponentially in time.

Fig. 2 presents the semi-axes of the ellipsoidal droplets as functions of the relative distance from the inner cylinder. The squared semi-axes of the droplets are equal to the real Eigenvalues of the symmetric tensor **S**,

$$\mu_{1,2} = \frac{1}{2}(S_{rr} + S_{\varphi\varphi}) \pm \sqrt{\frac{1}{4}(S_{rr} - S_{\varphi\varphi})^2 + S_{r\varphi}^2}, \tag{13a}$$

$$\mu_3 = S_{zz}, \tag{13b}$$

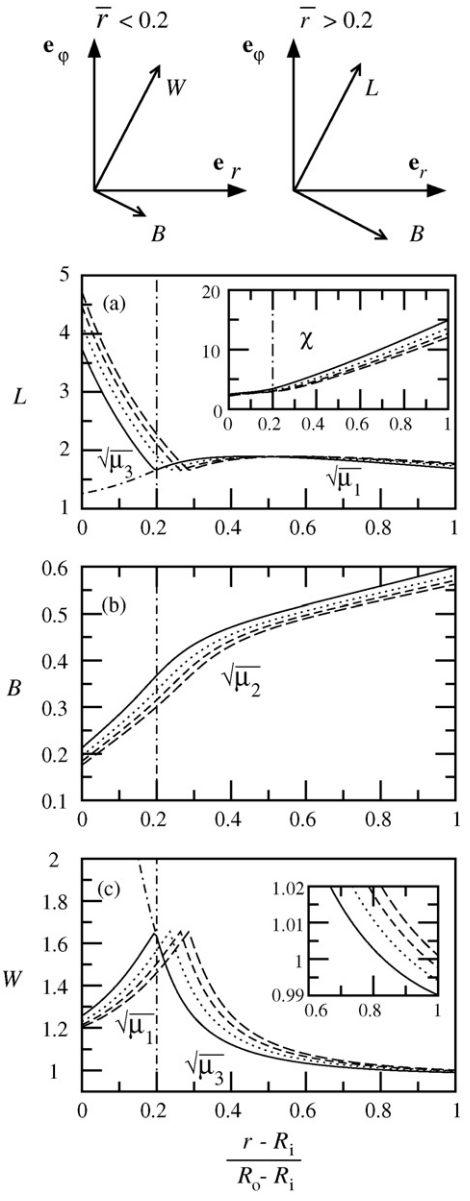

Fig. 2. The same as Fig. 1 for the semi-axes of ellipsoidal droplets: (a) major droplet axis, (b) minor droplet axis, and (c) intermediate droplet axis. Eigenvalues of the droplet shape tensor are denoted with each portion of the profiles, and the dot-dashed lines in (a) and (c) are the continuation of the Eigenvalue curves for $U_i = 0.3$. The dot-dashed vertical lines $\bar{r} = \bar{r}^* = 0.2$ denote the position of disc-like droplet configurations for $U_i = 0.3$. The insets show the orientation angle, χ, and the intermediate droplet axis, W, in the vicinity of the outer cylinder. The two drawings on top show schematically the Eigenvectors of the droplet shape tensor (labeled with the respective Eigenvalues) in the shearing ($\mathbf{e}_r\mathbf{e}_\varphi$) plane. The left illustration is for $\bar{r} < \bar{r}^*$ and the right one for $\bar{r} > \bar{r}^*$.

and the orientation angle of the droplets in the shearing plane is defined as

$$\chi = \frac{1}{2}\arctan\left(\frac{2S_{r\varphi}}{S_{\varphi\varphi} - S_{rr}}\right). \tag{13c}$$

The Eigenvectors corresponding to $\mu_{1,2}$ span the shearing plane and the Eigenvector corresponding to μ_3 points in the axial direction. We have calculated the Eigenvalues of the droplet shape tensor using a Jacobi transformation of the symmetric tensor $\mathbf{S}$. Note that μ_2 is the smallest Eigenvalue. However, the largest Eigenvalue is either μ_1 or μ_3 depending on the rate of deformation. From Figs. 2a and c, we note that near the outer cylinder μ_1 is the largest Eigenvalue, near the inner cylinder μ_3 is the largest Eigenvalue. The strong increase of μ_3 is consistent with sample calculations in Ref. ([5]; Fig. 6b). At radial position $\bar{r} = \bar{r}^*$, corresponding to the minima and absolute maxima in Figs. 2a and c, respectively, the Eigenvalues μ_1 and μ_3 are identical.

Fig. 2a displays the major droplet axis, L, Fig. 2b the minor droplet axis, B, and Fig. 2c the intermediate droplet axis, W. We should inspect first the qualitative behavior of the semi-axes as we move from the outer towards the inner cylinder; i.e., as shear rate increases. We do so exemplarily for the smallest value of inner cylinder rotation, U_i; i.e., the solid curves in Fig. 2. On the outer cylinder (the position of smallest shear rate) the major droplet axis is slightly larger than its equilibrium value of unity. As we move from the outer cylinder towards the inner, the major droplet axis increases slightly. This is intuitively clear as the shear rate increases with decreasing $\bar{r}$. For $\bar{r} \approx 0.44$, the major droplet axis assumes a relative maximum ($L \approx 1.89$) and then it decreases to a minimum at $\bar{r} = \bar{r}$ ($L \approx 1.66$). A non-monotonic behavior of the Eigenvalue μ_1, as observed between $\bar{r} = 1$ and $\bar{r}^*$, is also recovered for simple shearing flow ([5]; Fig. 6b). For $\bar{r} < \bar{r}^*$, the major droplet axis increases strongly to attain its absolute maximum on the inner cylinder ($L \approx 3.75$). Note that the derivative of the droplet profile is unsteady in the vicinity of its minimum at $\bar{r}^*$, because now μ_3 becomes the largest Eigenvalue.

The inset of Fig. 2a shows the orientation angle of the droplets in the shearing plane, which decreases monotonically from the outer towards the inner cylinder. Referring to the shearing plane, we find that droplets are less oriented near the outer cylinder ($\chi \approx 14.09$) than near the inner ($\chi \approx 2.49$). This is expected since shear rate increases monotonically from the outer to the inner cylinder.

Fig. 2b displays the minor droplet axis, B, which is always smaller than unity and decreases from the outer to the inner cylinder with increasing shear rate. Droplets are compressed in the direction of the Eigenvector corresponding to μ_2 since it is smaller than unity.

Fig. 2c displays the profile of the intermediate droplet axis, W, which is non-monotonic. As we move away from the outer cylinder, the intermediate droplet axis increases strongly and assumes values greater than unity. At $\bar{r} = \bar{r}^*$, a maximum occurs, and then a decrease as the inner cylinder is approached because now μ_1 is the intermediate Eigenvalue. The inset of Fig. 2c shows that W is smaller than unity at the outer cylinder for small and intermediate values of U_i.

We discuss next the orientation and shape of the droplets as we move from the outer cylinder towards the inner; i.e., as shear rate increases. Again, we discuss only the results for the smallest value of inner cylinder rotation, U_i, represented by the solid curves in Fig. 2. On the outer cylinder, droplet deformation is less pronounced with $L \approx 1.72$, $B \approx 0.60$, and $W \approx 0.99$. The major and the minor droplet axes lie in the shearing plane and the intermediate droplet axis points in the vorticity direction.

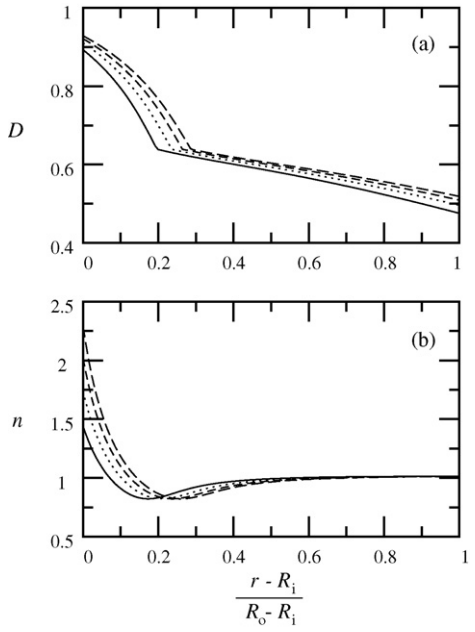

Fig. 3. The same as Fig. 1 for (a) the Taylor deformation parameter of the droplets and (b) the number density of droplets.

The orientation of the droplets with respect to the flow direction is already considerable ($\chi \approx 14.09$), although the shear rate assumes a relatively small value at the outer cylinder. Thus, at the outer cylinder, there is a prolate configuration with a pronounced asymmetry of the B- and the W-axes. We identify this as a cigar-shaped configuration, although the intermediate droplet axis is approximately at its equilibrium value of unity. As we move towards the inner cylinder, droplet deformation becomes more severe (cf. Fig. 3a). Between $\bar{r} = 1$ and $\bar{r} > \bar{r}^*$, we still observe cigar-shaped droplets; however, the asymmetry of the minor and the intermediate axes becomes larger compared to the outer cylinder. This is observed in Figs. 2b and c since B continues to decrease, whereas W increases rapidly. Note that the increase in W is balanced by the change of L to ensure incompressibility of the dispersed phase; i.e., $\det \mathbf{S} = 1$. For $\bar{r} = \bar{r}^*$, the major and the intermediate droplet axes attain the same values, and droplets assume configurations with $L = W \approx 1.66$. We identify this as a disc-like configuration with one major axis along the vorticity direction. As $\bar{r}$ is further decreased, the semi-axis corresponding to μ_1 becomes smaller than the semi-axis corresponding to μ_3. Now the largest droplet axis points into the axial direction. Furthermore, droplets also extend in the shearing plane since the two axes are greater than unity. At the inner cylinder, $L \approx 3.74$, $B \approx 0.21$, and $W \approx 1.25$, which represents a sheet-like configuration; i.e., the droplets are flat (B attains its minimum value) and they extend in the axial direction (L attains its maximum value). The orientation angle in the shearing plane has decreased; the W-axis is almost aligned with the flow field ($\chi \approx 2.49$). At the inner cylinder, the largest degree of droplet deformation occurs (cf. Fig. 3a).

We observe that the intermediate droplet axis, W, displays very interesting behavior with decreasing velocity gradient from the inner cylinder: it increases with increasing $\bar{r} < \bar{r}^*$ (i.e., droplets become more oblate, $W > 1$), and then obtains a maximum at about $\bar{r} = \bar{r}^*$, where droplets are disc-like $W = L$. Afterwards, for $\bar{r} > \bar{r}^*$, W returns to a value close to equilibrium (i.e., the droplets become less oblate without reaching a spherical shape). Note that we still have considerable droplet deformation at the outer cylinder since the material is sheared on that cylinder. The reason for the maxima and minima in the droplet shape profiles is therefore due to the switch from the major axis of the droplet at low shear rates lying in the plane of flow, to the major axis of the droplet shape aligning perpendicular to the flow plane at high shear rates. This is illustrated with the two coordinate systems in Fig. 2, which display the shearing plane together with the two Eigenvectors of $\mathbf{S}$ lying in that plane. For low shear rates (right coordinate system), the Eigenvector corresponding to the major Eigenvalue, L, lies in the shearing plane, whereas for high shear rates (left coordinate system), the Eigenvector of the intermediate Eigenvalue, W, lies in the shearing plane.

As the rotation speed of the inner cylinder is increased, the shear rate becomes higher throughout the gap, thus forcing the critical shear rate value for morphological inversion to occur closer to the outer cylinder. Furthermore, the orientation angle decreases with increasing inner cylinder rotation, meaning that droplets become more aligned as shear rates increase (cf. the inset of Fig. 3a). Concerning the magnitude of the intermediate droplet axis on the outer cylinder, we observe that it increases with U_i to attain a value of $W \approx 1.001$ for $U_i = 0.6$; i.e., it is larger than its equilibrium value (cf. the inset of Fig. 2c).

As to the reason for this morphological inversion of the direction of the principal axis, it is possible that the high value for G/Γ might play an important role, since the elasticity of the matrix phase dominates over the droplet interfacial energy. Consequently, the complicated force balance induced by the flow field between the matrix phase conformation and droplet deformation requires a re-direction of the preferred droplet orientation to minimize the system free energy beyond a critical value of the shear rate.[1] In this article, however, G/Γ is held constant, and the viscosity ratio, $p^\star$, is varied. As discussed more thoroughly below, this variable is also of interest in interpreting this phenomenon. For the value of $p^\star$ examined presently, $p^\star = -0.25$, the matrix phase viscosity dominates over the droplet viscosity in the low shear rate limit. At the critical value of the shear rate, the morphological inversion is induced once the viscosity of the shear-thinning matrix phase has been reduced to the point where the constant Newtonian droplet viscosity begins to dominate the system response. This is consistent with results for the $p^\star = -1.25$ blend, where the droplet viscosity is always higher than the matrix phase viscosity—see below. As already explained above, the minima in Fig. 2 are due to the ordering of the Eigenvalues of $\mathbf{S}$ with respect to their magnitude. Therefore, normal stress differences should not show a cusp at $\bar{r} = 0.2$ since

[1] Since the system is highly dissipative, the values of the phenomenological parameters will influence the flow field and the microstructural blend characteristics. However, the solutions obtained from the flow equations in local form (eq:pde) act to minimize the total system energy of the blend (according to the First Law of Thermodynamics) and result in a degradation of mechanical energy.

they are defined simply through the flow direction and the direction of its variation. We have not checked whether the change of droplet orientation affects the qualitative behavior of the normal stresses, as found for suspensions of rigid particles or liquid crystals.

Fig. 3 displays the Taylor droplet deformation parameter, $D = (L - B)/(L + B)$ (Fig. 3a), and the number density of droplets (Fig. 3b). The droplet deformation parameter is calculated directly from the semi-axes reported in Fig. 2, and the number density of droplets is obtained from solution of the number density Eq. (3e). The droplet deformation parameter is a decreasing function of the relative distance from the inner cylinder, implying that droplet deformation is larger near the inner cylinder and smaller near the outer cylinder. There is a noticeable inflection point in these curves within the annular gap, which is again associated with the switch in the direction of the major axis. The B axis deforms more when the principal axis lies in the perpendicular direction than it does when the major axis is in the plane of flow, as also evident in Fig. 2b.

Fig. 3b indicates that the number of droplets remains constant in the planar, oblate droplet regime, where the deformations are relatively small. However, once the droplets become aligned perpendicular to the plane of flow and extend significantly in that direction with decreasing $\bar{r}$, the number of droplets increases dramatically, more than doubling in number. This behavior is rather counter-intuitive, since one would expect increased deformation in the plane of shear to result in droplet break-up dominating the fluid microstructural changes, whereas for $\bar{r} > 0.4$, the number of droplets is approximately constant. Indeed, the small minima in the curves near $\bar{r} = 0.2$ implies that oblate droplets oriented parallel to the plane of flow tend to coalesce with increasing shear rate, and then experience a dramatic break-up behavior near the inner cylinder as the orientation shifts to the perpendicular plane. At the same time, the droplets are becoming very thin sheets, oriented perpendicularly to the flow plane.

The fact that droplets oriented perpendicularly to the shearing plane tend to break is not necessarily counter-intuitive if we consider purely Newtonian systems [11,15]. Indeed, for Newtonian liquids it is seen that flow stabilizes liquid threads because it damps capillary waves which arise due to velocity perturbations on the interface. However, in the absence of flow, e.g., after flow cessation, capillary waves can grow more readily, leading to break-up of extended liquid threads into many small droplets. In the vorticity direction of the concentric cylinder geometry there is no flow, and consequently capillary waves can grow more easily than in the shearing plane.

The effects of gap size on the respective profiles can be examined by changing the value of κ. The qualitative features of the velocity and shear rate profiles are very similar to those in Fig. 1. However, as κ increases, the value of the velocity increases quantitatively throughout the gap, since the inner cylinder is closer to the no-slip condition at the outer cylinder, $v_\varphi = 0$. Hence the quantitative values of the shear rate are also larger across the gap for smaller gap widths, and their values near to the outer cylinder decrease with increasing gap width. In Figs. 4 and 5, we present sample calculations for $\kappa = 0.7$, displaying the profiles

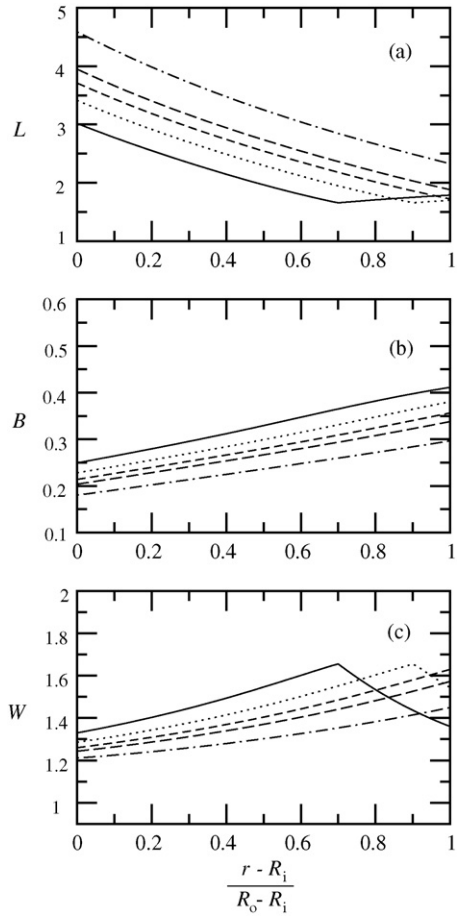

Fig. 4. The same as Fig. 2 for an annular gap of $\kappa = 0.7$. Results are displayed for the same model parameters as in Fig. 1, and values of the inner cylinder velocity are $U_i = 0.3$ (solid lines), 0.4 (dotted lines), 0.5 (dashed lines), and 0.6 (long-dashed lines). Dot-dashed lines are drop shape profiles for a larger value of the inner cylinder velocity, $U_i = 1.0$.

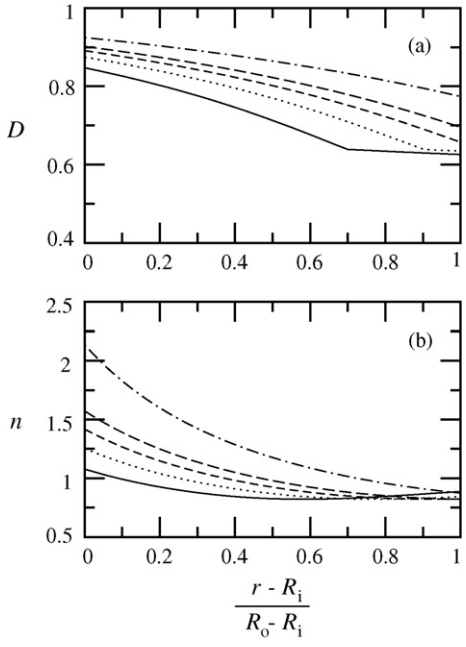

Fig. 5. The same as Fig. 4 for (a) the Taylor deformation parameter and (b) the number density of droplets.

of the semi-axes, the deformation parameter, and the number density. Sample calculations were performed for the same values of U_i as in Figs. 1–3. Additionally, we display profiles for $U_i = 1$, representing a maximum value of inner cylinder velocity where the TPBV problem is solvable for $\kappa = 0.7$ and $p^* = -0.25$.

Fig. 4, when compared with Fig. 2, displays the effects of gap size on the droplet axes for $\kappa = 0.7$; i.e., as gap size is decreased. For the axes, the qualitative features are the same as described above, except that the maxima and minima are pushed more toward the outer cylinder as κ increases. This is due to the fact that the shear rate increases near the outer cylinder with increasing κ. As the shear rate increases with increasing κ near to the outer cylinder, it enters the regime in which the droplets assume perpendicular orientations throughout the gap. Also, as κ increases, at the inner cylinder the major droplet axis decreases, whereas the other two semi-axes increase. Furthermore, for increasing κ, at the outer cylinder the minor droplet axis decreases further and the intermediate droplet axis increases since morphological inversion occurs near the outer cylinder. At the same time, as κ increases, Fig. 5 demonstrates that the number density of droplets is lower at both the inner and outer cylinders; however, the distribution in the number of droplets is more uniform across the gap for higher κ values. For larger gap widths, the majority of droplets congregate near the inner cylinder. Furthermore, note that the region of droplet coalescence in the range $0.2 < \bar{r} < 0.4$ when $\kappa = 0.3$ is almost eliminated as κ increases. For a small enough gap, it could be eliminated entirely.

Results thus far point to small gap widths for producing the most desirable droplet morphologies, assuming that one would prefer to have a uniform distribution of droplet density and the major axis of droplet orientation lying in the plane of shear. Although there are fewer droplets for the smaller gap widths and they are extended to a slightly lower degree, their distributions in number and shape are more uniform across the gap. However, one does not need to worry about possibly undesirable perpendicular orientations of droplet shapes forming near the outer cylinder if the gap is large enough, such that the shear rate throughout the gap is always in the disc-like regime. If uniformity of morphology is desired, then the best results are obtained in small gap Couette devices. The maximum degree of droplet morphological segregation is obtained at high rotation speeds of large gap devices. Clearly, these two parameters, gap width and rotation speed, can be used to optimize the two competing effects of uniformity of droplet number density, droplet deformation, and direction of orientation; in some applications, one might prefer highly deformed droplets, and in others, a more uniform distribution of slightly deformed droplets.

According to Fig. 4, $\kappa = 0.7$, i.e., $\delta = 0.3$ and $U_i = 0.6$, should be used to obtain a satisfactory droplet dispersion. For the set of model parameters used here, these values can be taken as a reference for process and geometrical parameters because they lead to small and uniform shear rates in the gap and many small droplets oriented in the axial direction. For $\delta = 0.3$ and larger values of U_i, more droplets can be generated at the cost of larger shear rates in the gap. For smaller values of U_i, shear rates become so low near the outer cylinder that droplets cannot orient in the axial direction, and consequently do not break in that region. Wider gaps lead to shear rate values which decrease rapidly near to the inner cylinder, which does not allow droplet break-up to occur since the drops cannot orient in the axial direction (cf. Fig. 2).

4.1.2. Large viscosity ratio blends

We next try to understand qualitatively the influence of the viscosity ratio on the morphological characteristics of polymer blends in the annular gap between two concentric cylinders. In the following description of results, the viscosity ratio is taken as $p^\star = -1.25$, which is substantially larger in magnitude than the previously used value of -0.25. In fact, this represents an inversion of the matrix phase and droplet phase viscosities, so that the droplet phase viscosity has now the larger value. We performed sample calculations for inner cylinder velocities between $U_i = 0.4$ and 1.0 for $\kappa = 0.5$ and $U_i = 1.0$ and 1.6 for $\kappa = 0.7$. This illustrates that, for $\kappa = 0.7$, the TPBV problem is solvable over a larger interval of inner cylinder velocities. In this article, convergence characteristics have not been investigated in detail for our model Eq. (3). The velocity and shear rate profiles as functions of $\bar{r}$ for rotation of the inner cylinder at various speeds and various κ values were calculated. The results are qualitatively similar to those described in the preceding subsection, with respect to variations of both $\bar{r}$ and κ, and so are not displayed here.

For the droplet axes, many of the qualitative trends described above are still evident in the model calculations—see Figs. 6 ($\kappa = 0.5$) and 7 ($\kappa = 0.7$). For examples shown here, the major axis increases with rotation speed across the gap, and the minor axis decreases, implying that the droplets become more deformed with increasing rotation speed. Furthermore, at a given rotation speed, the major axis is larger throughout the gap for larger values of κ. The minor axis shows the opposite trends. Hence the droplets are more deformed near the inner cylinder than near the outer one.

There are, however, some dramatic qualitative differences noticeable in Figs. 6c and 7c, with respect to their counterparts for the lower viscosity ratio of Figs. 2c and 4c. For the higher viscosity ratio blends, there is no evidence of oblate droplet shapes anywhere within the gap, as $W < 1$always. Consequently, there are no maxima and minima in the flow curves that are due to the switching of the direction of the major droplet axis—see Figs. 6a and c, and 8a. This is consistent with the previous results of Ref. [5] for this viscosity ratio. However, the vorticity axis does again display a minimum, which is pushed toward the outer cylinder as the rotation speed is increased and the gap width is decreased. This is purely a function of the shear rate value, as determined by the degree of coupling between the matrix and dispersed phases. At this higher inverted viscosity ratio where the droplet phase is the more viscous of the two, there is no significant force pushing the droplets out of the shear plane, and hence the droplets are prolate and lie in the flow plane. As the shear rate decreases with increasing $\bar{r}$ across the gap, even though the droplets are always prolate, they become more prolate, and then less prolate, with

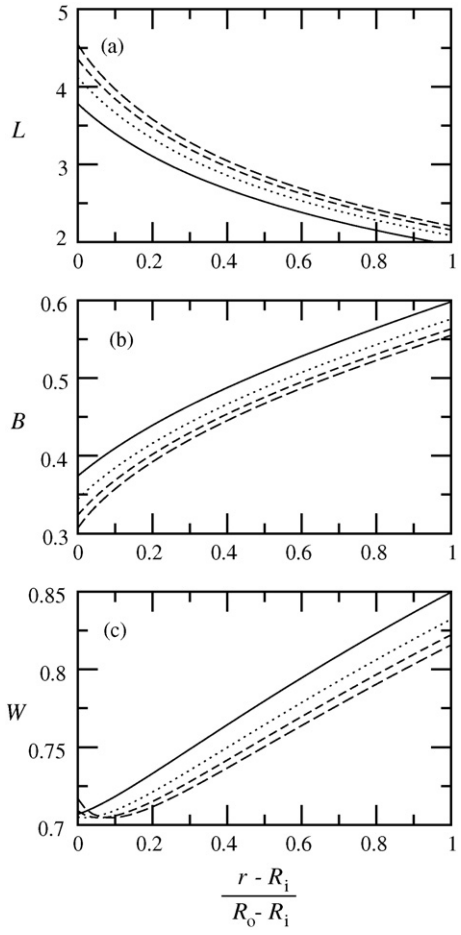

Fig. 6. Droplet shape profiles for the $p^* = -1.25$ polymer blend in the annular gap $\kappa = 0.5$ for four inner cylinder velocities: $U_i = 0.4$ (solid lines), 0.6 (dotted lines), 0.8 (dashed lines), and 1.0 (long-dashed lines). Other model parameters are $\phi = 0.1$, $G/\Gamma = 4$, $\lambda_C\lambda_S/\lambda_n^2 = 1$, $\theta = 0.1$, and $k = -2$. (a) Major droplet axis, (b) minor droplet axis, and (c) intermediate droplet axis.

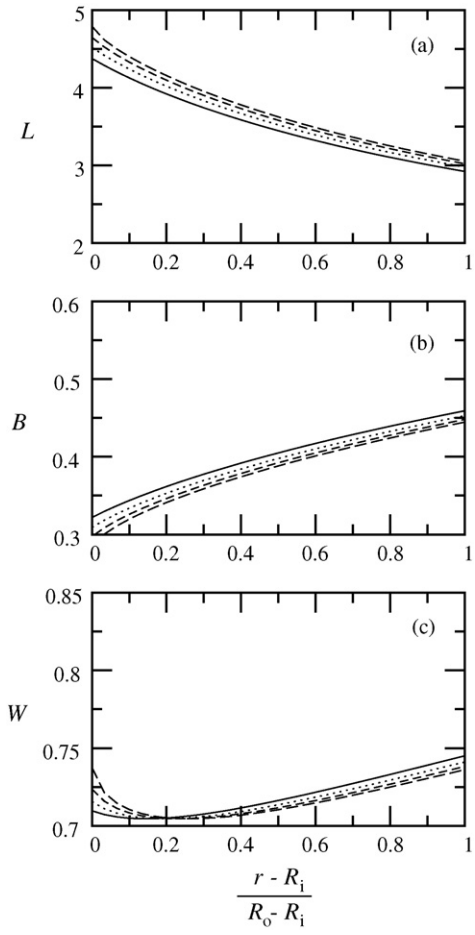

Fig. 7. The same as Fig. 6 for $\kappa = 0.7$ and $U_i = 1.0$ (solid lines), 1.2 (dotted lines), 1.4 (dashed lines), and 1.6 (long-dashed lines).

the cross-over point (corresponding to the minimum in the W curve) being pushed to larger radial values with increasing gap width.

The modeling of viscoelastic fluids requires several independent length scales related to the flow field and the thermodynamic properties of the fluid. With the flow Eq. (3), we introduced three length scales. First is the length scale of the flow field determined by the gap width of the concentric cylinders. Second is the length scale of the matrix microstructure, which is determined by the characteristics of the polymer configurations. Third is the scale of the droplets given by their equilibrium diameter. Consequently, microstructural length scales depend on the polymer blend and flow length scales are specified by the geometry of the flow field. Therefore, it is not possible to relate the major droplet axis in Fig. 6a, $L \approx 5$ (dimensionless units), to the circumference of the inner cylinder, π (dimensionless units). To recover the correct dimensional quantities, the length scales of the material and the flow geometry have to be introduced explicitly, as already explained above.

The droplet deformation parameter is displayed in Fig. 8a for a gap width of $\kappa = 0.7$ and several rotation rates. The num-

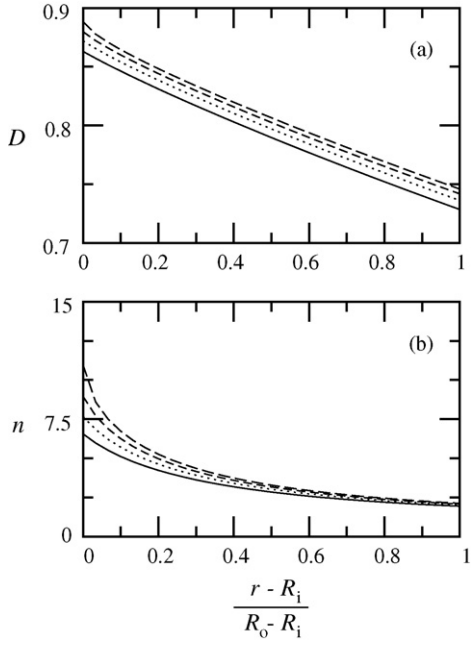

Fig. 8. The same as Fig. 7 for (a) the Taylor deformation parameter and (b) the number density of droplets.

ber density of droplets is displayed in Fig. 8b. The qualitative features of these graphs are independent of gap width. The deformation parameter, D, has the expected behavior of decreasing with radial coordinate, and increasing with rotation speed. The qualitative features are the same as for the material with the low viscosity ratio; however, the value of D is less for the material with the high viscosity ratio, for comparable cylinder rotation rates, although only slightly. The major difference between the two viscosity ratio blends lies in the number of droplets: the material with the higher viscosity ratio has a factor of 3 more droplets throughout the gap than the low viscosity ratio blend, indicating a more dramatic degree of droplet break-up. Furthermore, the number of droplets increases marginally as the gap width increases, although their distribution across the gap is rather independent of κ. One might have intuitively expected that the lower viscosity ratio blend would have a higher degree of break-up (as known for blends of Newtonian liquids [16]); however, it is rather the interfacial energy that determines the break-up process. For constant interfacial energy, as is the case here, the higher viscosity ratio blend suffers more break-up since this blend has a larger force applied to it at an equivalent shear rate value (due to the larger shear stress associated with the higher droplet viscosity). This trend is in contrast to the behavior of blends of Newtonian liquids [16], where droplet break-up vanishes as the viscosity ratio approaches values between three and four. A direct comparison of the calculations with data in Refs. [16,12,11] is critical, however, because we consider non-Newtonian flow behavior of the matrix phase and the interface. Matrix and interfacial elasticity are essential parts of the model, and we believe that these properties alter significantly the dispersion characteristics in the concentric cylinder device. Note that the viscosity ratio enters quadratically into the flow equations, which makes it more difficult to perform the calculations at large viscosity ratios. This might be a critical point to be adjusted by redefining the phenomenological coefficients related to the dissipative contributions of the flow equations.

If our goal is to maximize the number of droplets in the model polymer blend, and to have orientation in the plane of shear, then these results clearly indicate that in the Couette geometry, it is better to have a blend in which the droplet phase has a higher viscosity than the matrix phase. After this overriding constraint, it is apparent that one would prefer narrower gaps for this blend since there is a greater number of droplets produced in the narrower gap, and since the drop distribution does not change much with gap size.

4.2. Co-rotating cylinders for large viscosity ratio blends

Thus far, it appears that the preferred choice of polymer blends are those in which the viscosity of the droplet phase is larger than that of the matrix phase. Consequently, in the remaining sections of this manuscript, we will only examine the blend with the larger viscosity ratio value of -1.25. In this section, we will examine the morphological characteristics of the model blend in a geometry composed of co-rotating concentric cylinders.

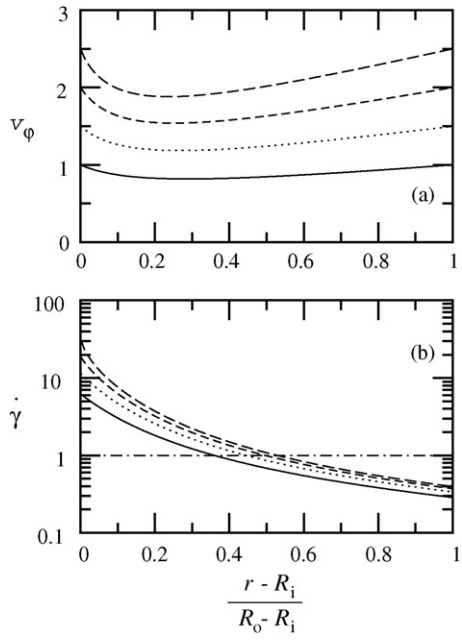

Fig. 9. Couette flow profiles for the $p^* = -1.25$ polymer blend in the annular gap $\kappa = 0.5$ with co-rotating cylinders: $U_i = 1.0$ (solid lines), 1.5 (dotted lines), 2.0 (dashed lines), and 2.5 (long-dashed lines). Other model parameters are the same as in Fig. 6. (a) Circular velocity and (b) corresponding shear rate. The dot-dashed horizontal line is a guide to the eye to show zones with shear rates smaller and larger than unity.

The velocity fields for two values of gap width are displayed in Figs. 9a ($\kappa = 0.5$) and 10a ($\kappa = 0.7$), and the shear rate profiles are presented in Figs. 9b and 10b. We assume that the two cylinders are rotating in the same direction, and at the same speed. As κincreases, it is evident from these figures that both the

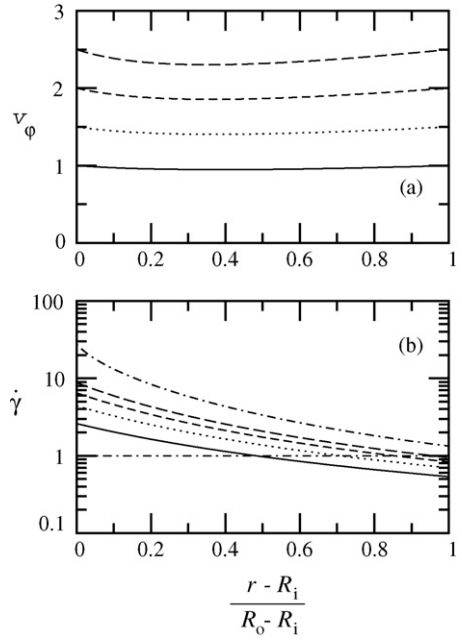

Fig. 10. The same as Fig. 9 for $\kappa = 0.7$ and $U_i = 1.0$ (solid lines), 1.5 (dotted lines), 2.0 (dashed lines), and 2.5 (long-dashed lines). The dot-dashed profile is for $U_i = 5.0$ to illustrate that the TPBV problem can be solved computationally beyond 2.5.

velocity and shear rate profiles become more uniform throughout the annular region. For the small κ value, there is a very distinct minimum in the velocity profile, which is caused by the retarding viscous response of the blend; i.e., the fluid is dragged along by the rotating cylinders, since the no-slip condition is applied at each cylinder. As the rotation rate increases, the minima in the velocity profiles become more severe. These minima occur very close to the inner cylinder at large gap widths, but lessen in severity and creep toward the middle of the annulus as the gap width decreases. This is because of the balance between the shear and centrifugal forces: the latter push the velocity profiles to larger radial dimensions, and hence the profiles are weighted toward the outer side of the gap. For the large κ value, the velocity profiles become nearly plug-like, with a very smooth distribution across the gap.

Figs. 9b and 10b show the shear rate profiles across the gap in a semi-logarithmic representation. We see that shear rates are not uniform across the gap but vary over more than an order of magnitude. The horizontal dot-dashed lines are introduced as a guide to the eye to display zones with shear rates above and below unity. Everywhere in the gap the shear rate, Eq. (10), is non-zero, which is consistent with non-spherical droplet shapes throughout the gap (cf. Fig. 11). An examination of the shear rate profiles in a linear representation reveals that they are very steep near the inner cylinder due to the large velocity change that occurs in its vicinity. Fig. 9b shows, e.g., that for $U_i = 2.5$ the shear rates vary between 32.10 and 1.0 in the inner part of the geometry ($\bar{r} < 0.5$) and between 1.0 and 0.40 in the outer part. For the large κ value (cf. Fig. 10b), the shear rate decreases at the inner cylinder and increases at the outer cylinder to yield a more uniform profile. In Fig. 10b, we include the shear rate profile for $U_i = 5$ as a dot-dashed line to illustrate that the profile does not change qualitatively if the inner cylinder velocity is further increased. For $\kappa = 0.7$ and $p^* = -1.25$, $U_i = 0.5$ is approximately the largest value which allows us to solve the TPBV problem.

The profiles of the droplet axes are displayed in Fig. 11 for the smallest gap width, $\kappa = 0.7$. We show sample calculations for larger values of inner cylinder velocities (between $U_i = 2.0$ and 5.0) to illustrate that, near the inner cylinder, the profiles of the intermediate droplet axis become non-monotonic. The plots for all gap widths are qualitatively and quantitatively similar to those from the previous section where the outer cylinder was stationary. All gap width effects are as reported there. The primary difference between the two cases is that the axes of the co-rotating cylinders geometry have a wider range of values at any radial position as functions of the rotation speed. This wider distribution allows for a higher degree of control when attempting to fine-tune blend morphological characteristics.

The most significant difference between the stationary outer cylinder and co-rotating cylinder geometries is with regard to

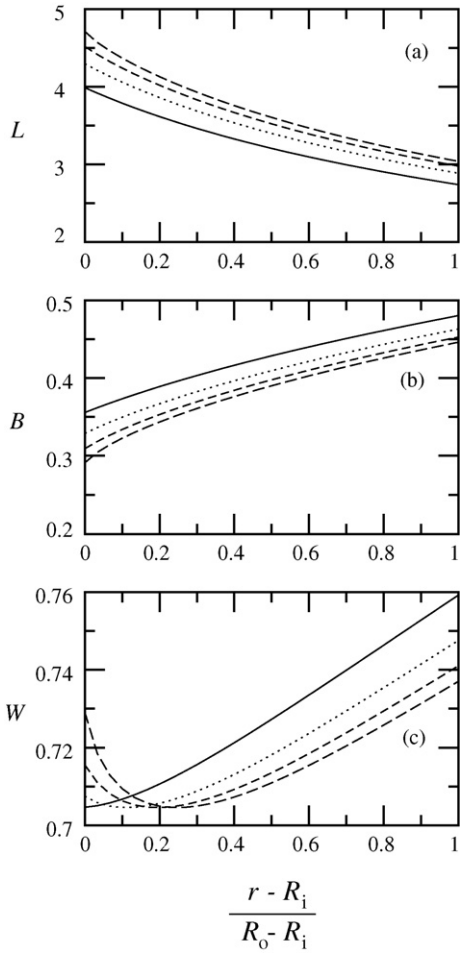

Fig. 11. The same as Fig. 10 for the semi-axes of ellipsoidal droplets and larger values of inner cylinder velocity: $U_i = 2.0$ (solid lines), 3.0 (dotted lines), 4.0 (dashed lines), and 5.0 (long-dashed lines). (a) Major droplet axis, (b) minor droplet axis, and (c) intermediate droplet axis.

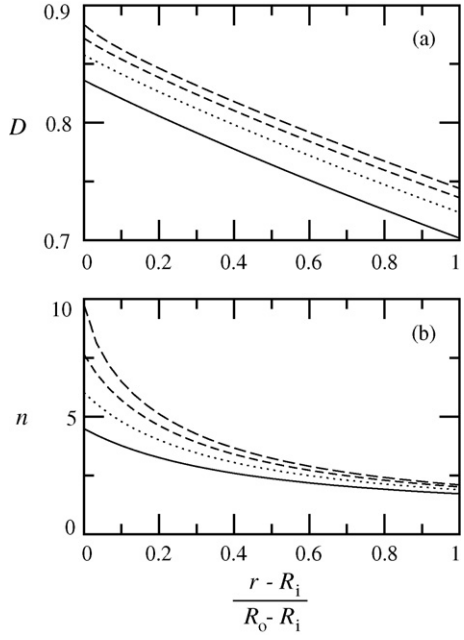

Fig. 12. The same as Fig. 10 and larger values of inner cylinder velocity: $U_i = 2.0$ (solid lines), 3.0 (dotted lines), 4.0 (dashed lines), and 5.0 (long-dashed lines). (a) The Taylor deformation parameter and (b) the number density of droplets.

the number density of droplets, as depicted in Fig. 12. Again, the smallest gap width produces the maximum number of droplets within the annular region, as well as the smoothest distribution with respect to the radial coordinate. It is thus possible to conclude that the co-rotating cylinder geometry is preferred over the stationary outer cylinder geometry for the intelligent design and control of blend morphology, unless one specifically desires oblate droplet shapes lying perpendicular to the flow plane, rather than prolate ones lying within it.

4.3. Counter-rotating cylinders for large viscosity ratio blends

In this section, we very briefly examine counter-rotating cylinders, which are rotating at equivalent speeds in opposite directions. Again, the smallest gap produces the most desirable morphological characteristics, so we concentrate on this case only. The velocity and shear rate profiles exhibited in Fig. 13 are very similar qualitatively to the co-rotating geometry, except that presently the velocity profiles at different rotation rates become more concentrated in distribution as the gap width decreases, which is opposite to the trend in the co-rotating case. All other characteristics of these profiles are essentially the same as in the co-rotating case. Consequently, the droplet axes are also more narrowly distributed throughout the gap, as illustrated in Fig. 14; however, all of the qualitative characteristics are again the same as for the co-rotating geometry. The most interesting feature of the counter-rotating case is that it produces the greatest number of droplets at the lowest rotation speeds of any of the three cases examined in this article—see Fig. 15. However, this

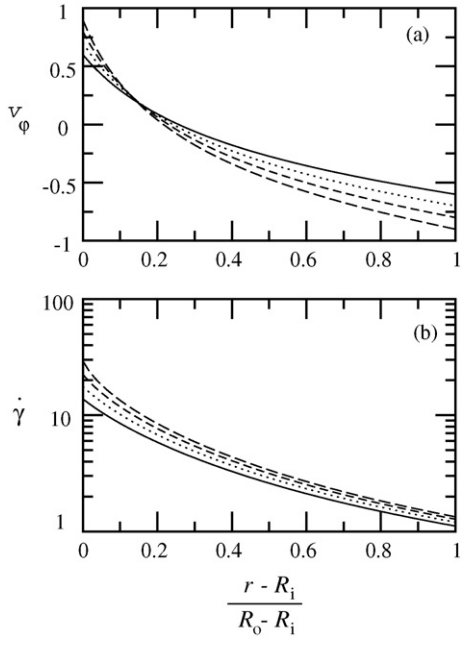

Fig. 13. Couette flow profiles for the $p^* = -1.25$ polymer blend in the annular gap $\kappa = 0.7$ with counter-rotating cylinders: $U_i = 0.6$ (solid lines), 0.7 (dotted lines), 0.8 (dashed lines), and 0.9 (long-dashed lines). Other model parameters are the same is in Fig. 6. (a) Circular velocity and (b) corresponding shear rate.

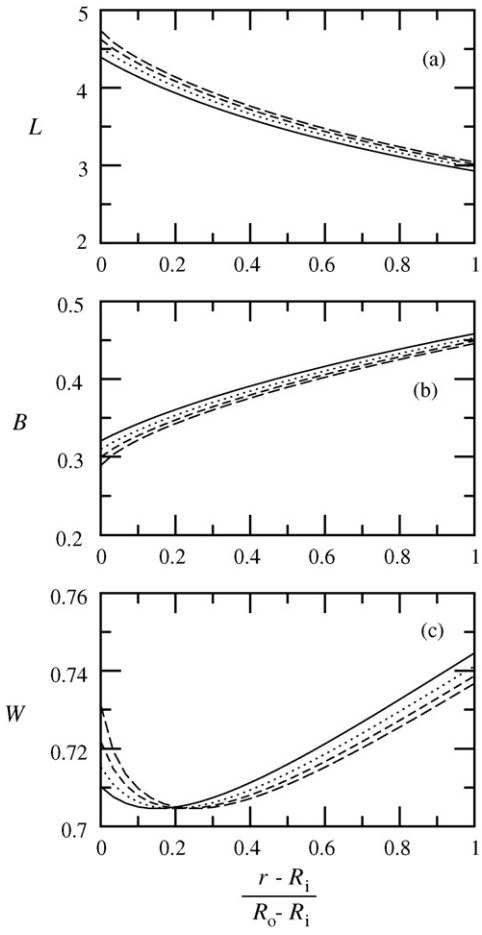

Fig. 14. The same as Fig. 13 for the semi-axes of ellipsoidal droplets. (a) Major droplet axis, (b) minor droplet axis, and (c) intermediate droplet axis.

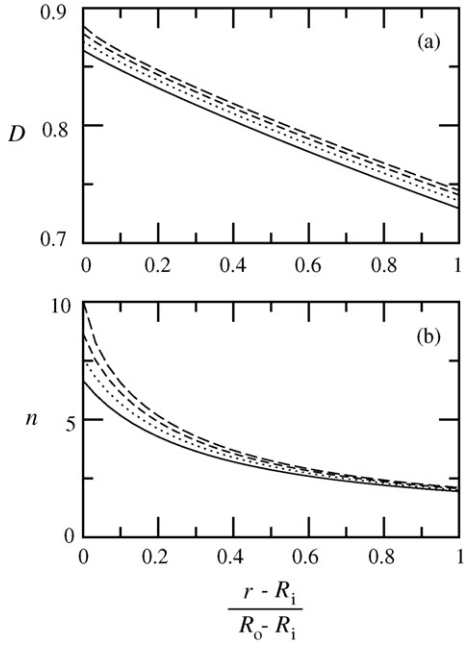

Fig. 15. The same as Fig. 13 for (a) the Taylor deformation parameter and (b) the number density of droplets.

advantage is mitigated by the fact that the distribution of number density across the gap is less uniform than in the co-rotating case.

5. Discussion and conclusions

In conclusion, it is apparent that small gap devices are the preferred geometries for inducing droplet break-up into a large number of micro-droplets. Which type of rotational geometry is preferred, co-rotating, counter-rotating, or stationary outer cylinder, depends on the tolerance limitations of the process design. For slow flows, the counter-rotating device is preferred for inducing the formation of the largest number of droplets, but one pays the price of having a rather severe distribution of droplet sizes across the gap. If one can generate high enough rotational speeds, the co-rotating cylinder geometry can produce the same number of droplets, with more uniform distributions of size and shape across the gap. In either case, material parameters, such as the viscosity ratio, relaxation times, etc., can be used to design the specific blend for specified process conditions to produce the desired blend microstructure, providing one has an accurate model of the polymer blend dynamics. Of course, no such model yet exists; however, much can be learned from examining the dynamical behavior of the models which do exist, under realistic processing conditions. Thus, the primary focus of this article was to demonstrate how one might begin to simulate flow processes of these very complicated systems of partial differential equations for polymer blend dynamics under inhomogeneous flow conditions.

Acknowledgment

Financial support was provided by the Swiss National Science Foundation (200021-105463/1 and 200021-111844/1).

References

[1] M. Doi, T. Ohta, Dynamics and rheology of complex interfaces, J. Chem. Phys. 95 (1991) 1242–1248.
[2] N.J. Wagner, H.C. Öttinger, B.J. Edwards, Generalized Doi–Ohta model for multiphase flow developed via GENERIC, AICHE J. 45 (1999) 1169–1181.
[3] P.L. Maffettone, M. Minale, Equation of change for ellipsoidal drops in viscous flow. Erratum (1999) 84:105–106, J. Non-Newtonian Fluid Mech. 78 (1998) 227–241.
[4] M. Grmela, M. Bousmina, J.F. Palierne, On the rheology of immiscible blends, Rheol. Acta 40 (2001) 560–569.
[5] M. Dressler, B.J. Edwards, The influence of matrix viscoelasticity on the rheology of polymer blends, Rheol. Acta 43 (2004) 257–282.
[6] M. Dressler, B.J. Edwards, Rheology of polymer blends with matrix-phase viscoelasticity and a narrow droplet size distribution, J. Non-Newtonian Fluid Mech. 120 (2004) 189–205.
[7] A.S. Almusallam, R.G. Larson, M.J. Solomon, A constitutive model for the prediction of ellipsoidal droplet shapes and stresses in immiscible blends, J. Rheol. 44 (2000) 1055–1083.
[8] M. Dressler, B.J. Edwards, A method for calculating rheological and morphological properties of constant-volume polymer blend models in inhomogeneous shear fields, J. Non-Newtonian Fluid Mech. 130 (2005) 77–95.
[9] M. Dressler, B.J. Edwards, Channel, Tube, and Taylor-Couette flow of complex viscoelastic fluid models, Rheol. Acta 46 (2006) 59–82.
[10] A. Braun, M. Dressler, E.J. Windhab, Polymer blend flow in the conveying zone of single screw extruders, J. Non-Newtonian Fluid Mech. 149 (2008) 93–103.
[11] G.I. Taylor, The formation of emulsions in definable fields of flow, Proc. R. Soc. Lond. Ser. A 146 (1934) 501–523.
[12] R.G. Cox, The deformation of a drop in a general time-dependent fluid flow, J. Fluid Mech. 37 (3) (1969) 601–623.
[13] S.J. Choi, W.R. Schowalter, Rheological properties of nondilute suspensions of deformable particles, Phys. Fluids 18 (4) (1975) 420–427.
[14] L. Rayleigh, On the capillary phenomena of jets, Proc. R. Soc. Lond. Ser. A 29 (1879) 71–97.
[15] S. Tomotika, Breaking of a drop of viscous liquid immersed in another viscous fluid which is extending at a uniform rate, Proc. R. Soc. Lond. Ser. A 153 (1935) 302–318.
[16] H.P. Grace, Dispersion phenomena in high viscosity immiscible fluid systems and application of static mixers as dispersion devices in such systems, Chem. Eng. Commun. 14 (1982) 225–277.
[17] J.J. Elmendorp, A study on polymer blending microrheology, Polym. Eng. Sci. 26 (1986) 418–426.
[18] A.N. Beris, B.J. Edwards, Thermodynamics of Flowing Systems, Oxford University Press, New York, 1994.
[19] B.J. Edwards, A.N. Beris, Noncanonical Poisson bracket for nonlinear elasticity with extensions to viscoelasticity, J. Phys. A-Math. Gen. 24 (1991) 2461–2480.
[20] B.J. Edwards, A.N. Beris, Unified view of transport phenomena based on the generalized bracket formulation, Ind. Eng. Chem. Res. 30 (1991) 873–881.
[21] H.C. Öttinger, M. Grmela, Dynamics and thermodynamics of complex fluids. II. Illustrations of a general formalism, Phys. Rev. E 56 (1997) 6633–6655.
[22] A. Souvaliotis, A.N. Beris, Applications of domain decomposition spectral collocation methods in viscoelastic flows through model porous-media, J. Rheol. 36 (1992) 1417–1453.
[23] B.J. Edwards, M. Dressler, M. Grmela, A. Aït-Kadi, Rheological models with microstructural constraints, Rheol. Acta 42 (2003) 64–72.
[24] R.I. Tanner, Engineering Rheology, 2nd edition, Oxford University Press, New York, 2000.
[25] R.B. Bird, R.C. Armstrong, O. Hassager, Dynamics of Polymeric Liquids: Fluid Mechanics, vol. 1, John Wiley & Sons Inc., New York, NY, U.S.A., 1987, nebis Signatur: 434 119: 1.
[26] W.H. Press, S.A. Teukolsky, W.T. Vetterling, B.P. Flannery, Numerical Recipes, 2nd edition, Cambridge University Press, 1992.
[27] R.G. Larson, E.S. Shaqfeh, S.J. Muller, A purely elastic instability in Taylor–Couette flow, J. Fluid Mech. 218 (1990) 573–600.